

Density matrix renormalization group study of a three-orbital Hubbard model with spin-orbit coupling in one dimension

Nitin Kaushal,^{1,2} Jacek Herbrych,^{1,2} Alberto Nocera,^{1,2} Gonzalo Alvarez,^{3,4} Adriana Moreo,^{1,2} F. A. Reboredo,² and Elbio Dagotto^{1,2}

¹*Department of Physics and Astronomy, The University of Tennessee, Knoxville, Tennessee 37996, USA*

²*Materials Science and Technology Division, Oak Ridge National Laboratory, Oak Ridge, Tennessee 37831, USA*

³*Center for Nanophase Materials Sciences, Oak Ridge National Laboratory, Oak Ridge, Tennessee 37831, USA*

⁴*Computational Science and Engineering Division,*

Oak Ridge National Laboratory, Oak Ridge, Tennessee 37831, USA

(Dated: April 25, 2022)

Using the Density Matrix Renormalization Group technique we study the effect of spin-orbit coupling on a three-orbital Hubbard model in the $(t_{2g})^4$ sector and in one dimension. Fixing the Hund coupling to a robust value compatible with some multiorbital materials, we present the phase diagram varying the Hubbard U and spin-orbit coupling λ , at zero temperature. Our results are shown to be qualitatively similar to those recently reported using the Dynamical Mean Field Theory in higher dimensions, providing a robust basis to approximate many-body techniques. Among many results, we observe an interesting transition from an orbital-selective Mott phase to an excitonic insulator with increasing λ at intermediate U . In the strong U coupling limit, we find a non-magnetic insulator with an effective angular momentum $\langle (\mathbf{J}^{eff})^2 \rangle \neq 0$ near the excitonic phase, smoothly connected to the $\langle (\mathbf{J}^{eff})^2 \rangle = 0$ regime. We also provide a list of quasi-one dimensional materials where the physics discussed in this publication could be realized.

I. INTRODUCTION

The study of iridates continues attracting considerable attention. In layered materials such as Sr_2IrO_4 and Ca_2IrO_4 , involving $5d$ electrons, the Hubbard repulsion is moderate as compared to $3d$ electrons because the size of the associated wave functions is larger for the $5d$ sector [1–8]. In addition, as we move down in the periodic table the strength of the spin-orbit coupling (SOC) increases as Z^4 , with Z as the atomic number, and it can become of order 0.4 eV for some $4d$ or $5d$ materials. As a consequence, iridates provide an interesting playground where the Hubbard repulsion and SOC are of similar magnitudes [9]. In these iridates the t_{2g} orbitals split into a total angular momentum (half-filled) doublet $j = 1/2$ and a (fully occupied) quartet $j = 3/2$ [10].

More recently, interest also developed in other transition metal oxides with octahedron or distorted octahedron crystal-field splittings leading to $(t_{2g})^4$ ions [10–24]. When the Hubbard U and Hund J_H couplings are large it is expected that the system develops $S = 1$ states, while increasing the SOC λ should lead to states with an effective angular momentum zero. Thus, the next obvious step is to understand the phases in these systems in the presence of hopping. Experiments on these materials have shown contrasting results thus far. For example, the magnetic properties of Sr_2YIrO_6 [19] suggest exotic antiferromagnetic (AFM) ordering coming from excitonic condensation, while other experiments [20] favor a nonmagnetic ground state. Double perovskites such as Ba_2YIrO_6 are also challenging to study [21, 22]. This situation demands a comprehensive and accurate theoretical study of the combined effects of U and λ in the $(t_{2g})^4$ sector.

Alongside the iridates, progress has been made on iron-based superconductors in recent years [25–27]. While initially the expectation was that weak coupling approximations and Fermi surface nesting between hole and electron pockets could be sufficient to understand these compounds, recent efforts have highlighted the importance of Hubbard interactions of at least intermediate value between weak and strong coupling [28]. For example, there are materials that do not have hole pockets, yet they still superconduct [29]. Moreover, via angle-resolved photoemission spectroscopy (ARPES) it has been argued [30] that a SOC of order 20 meV, much smaller than in iridates, may still influence the features of the Fermi level and thus affect superconducting properties.

Considering all these challenging fields of research, and their common focus on intermediate range Hubbard U and spin-orbit coupling λ interactions, in this publication employing numerically exact computational techniques we will study a model of interacting electrons in the simultaneous presence of nonzero U , λ , and J_H . In particular, we will analyze a multiorbital model defined on a one dimensional geometry.

Our study is conceptually generic but for simplicity will focus on a previously used three-orbital Hubbard model with bands that resemble layered iron superconductors, containing hole and electron pockets. In the absence of spin-orbit coupling, this model was studied before via the Density Matrix Renormalization Group (DMRG) technique and a rich phase diagram was observed, including an orbital-selective Mott phase (OSMP), where two orbitals are partially filled and thus they are metallic, while the other orbital is half-filled and behaves like a Mott insulator [31–34]. Our main focus is to analyze how this phase diagram is modified after including atomic spin-orbit effects. The generic analysis

reported here is important for three reasons:

(i) By constructing the phase diagram in one dimension including the combined effects of the Hubbard interaction U as well as the spin-orbit coupling λ with a robust computational technique, we can address the accuracy of previous approximate studies performed in higher dimensions. For example, recently Dynamical Mean Field Theory (DMFT) calculations were performed [35–37] on a three-orbital Hubbard model with degenerate t_{2g} orbitals and four electrons per site. Their analysis showed the presence in the phase diagram of an interesting excitonic condensate (to be described below) and a non-magnetic insulator with zero effective total angular momentum. Our accurate numerical results on chains using non-cubic t_{2g} bands confirm most of the DMFT predictions, including the existence of an excitonic condensate, thus suggesting that studies in different dimensions may lead to qualitatively similar results.

(ii) There are real materials with quasi-one dimensional characteristics where spin-orbit effects are expected to be important. For example, recently, single-crystals of $\text{Ba}_5\text{AlIr}_2\text{O}_{11}$ that contain dimer chains were experimentally studied [38]. This is a Mott insulator with a subtle structural transition at $T_S = 210$ K and a magnetic transition at much lower temperatures. A novel and intriguing magnetic state was reported, that is neither $S = 3/2$ nor $J = 1/2$ but instead intermediate between them. Other examples of spin-chain $4d$ - and $5d$ -based compounds are $\text{Sr}_5\text{Rh}_4\text{O}_{12}$, $\text{Ca}_5\text{Ir}_3\text{O}_{12}$, and Ca_4IrO_6 [39]. These are insulators characterized by partial AFM order at low temperatures. $\text{Sr}_3\text{CuIrO}_6$ is also a quasi-one dimensional material where IrO_6 octahedra are linked by spin-1/2 Cu ions along one direction [40]. In this compound intersite hopping is suppressed by the geometry of the system locating $\text{Sr}_3\text{CuIrO}_6$ in the strongly localized regime, with a noncubic crystal-field comparable in strength to the spin-orbit coupling. Other examples of interesting one dimensional systems where our results may be of relevance are BaIrO_3 [41, 42], CaIrO_3 [43], $\text{Sr}_3\text{M}(\text{IrO}_6)$ ($M = \text{Ni}, \text{Cu}, \text{Zn}$) [44], lead iodides [45], and alkaline-earth palladates [46].

(iii) As already explained, recent ARPES measurements reported a sizable spin-orbit splitting in all the main members of the iron-based superconductors family [30]. This spin-orbit coupling affects the low-energy electronic structure and, thus, may have implications for superconductivity. While the magnitude of λ for iron pnictides and chalcogenides is substantially smaller than for iridates, it is conceptually interesting to investigate what kind of phases could be found if members of the iron superconductors family would have a larger λ .

Spin-orbit effects are often discarded in the literature, usually by hand waving arguments, and the models are largely simplified as a result. But realistic detailed studies involving spin-orbit couplings comparable to other small energies of interest (such as the magnetic superexchange J) are lacking. Moreover, it is experimentally challenging to determine the precise magnitude of spin-

orbit contributions. On the *ab-initio* side of theory, often these spin-orbit contributions are not considered if expected to be smaller than systematic errors in the approach, typically of order 0.5 eV. As a consequence, an evaluation of the effects of spin-orbit corrections on the results of specific models could determine if refined *ab-initio* or measurements are required.

The organization of this manuscript is as follows. In Sec. II, the model used and the computational methodology are presented. In Sec. III, the main results, particularly the phase diagram varying U and λ , are shown. In particular, we address three regimes: weak, intermediate, and strong Hubbard interaction U . In Sec. IV, we discuss the results and present our conclusions.

II. MODEL AND METHOD

In this study we have used a one dimensional three-orbital Hubbard model. The Hamiltonian contains a tight-binding term, an on-site Hubbard interaction, and a spin-orbit coupling: $H = H_K + H_{\text{int}} + H_{\text{SOC}}$. The electronic kinetic energy component is

$$H_K = - \sum_{i,\sigma,\gamma,\gamma'} t_{\gamma\gamma'} (c_{i\sigma\gamma}^\dagger c_{i+1\sigma\gamma'} + \text{h.c.}) + \sum_{i,\sigma,\gamma} \Delta_\gamma n_{i\sigma\gamma}. \quad (1)$$

The hopping amplitudes $t_{\gamma\gamma'}$ are defined in orbital space and they connect the nearest-neighbor lattice sites i and $i + 1$, with the specific values (in eV units) $t_{00} = t_{11} = -0.5$, $t_{22} = -0.15$, and $t_{\gamma\gamma'} = 0$ if $\gamma \neq \gamma'$. The total bandwidth is $W = 4.33 |t_{00}|$. The above mentioned 0, 1, and 2 orbitals can be visualized as representing the canonical d_{yz} , d_{xz} , and d_{xy} orbitals, respectively. The orbital-dependent crystal-field splitting is denoted by Δ_γ , with $\Delta_0 = -0.05$, $\Delta_1 = -0.05$, and $\Delta_2 = 0.8$ (also in eV units). The band structure of this model qualitatively resembles that of iron-based superconductors, i.e., hole and electron pockets centered at wavevectors $q = 0$ and π , respectively. A very similar band structure was used in our previous studies for a three-orbital Hubbard model [31–34], where OSMF was analyzed. This previous work was carried out in the absence of spin-orbit interactions, and our main focus is to analyze the effects of this additional term in the model. The Hubbard portion of the Hamiltonian includes the following onsite components in the standard notation

$$\begin{aligned} H_{\text{int}} = & U \sum_{i,\gamma} n_{i\uparrow\gamma} n_{i\downarrow\gamma} + (U' - J_H/2) \sum_{i,\gamma<\gamma'} n_{i\gamma} n_{i\gamma'} \\ & - 2J_H \sum_{i,\gamma<\gamma'} \mathbf{S}_{i\gamma} \cdot \mathbf{S}_{i\gamma'} + J_H \sum_{i,\gamma<\gamma'} (P_{i\gamma}^\dagger P_{i\gamma'} + \text{h.c.}). \end{aligned} \quad (2)$$

In this expression the operator $\mathbf{S}_{i\gamma} = \frac{1}{2} \sum_{\alpha,\beta} c_{i\alpha\gamma}^\dagger \boldsymbol{\sigma}_{\alpha\beta} c_{i\beta\gamma}$ is the total spin at orbital γ and lattice site i , and $n_{i\gamma}$ is the electronic density at each orbital. The first two terms describe the intra- and inter-orbital electronic repulsion,

respectively. The third term contains the Hund coupling that favors the ferromagnetic alignment of the spins at different orbitals; the fourth term is the pair hopping with $P_{i\gamma} = c_{i\downarrow\gamma}c_{i\uparrow\gamma}$ as the pair operator. We use the standard relation $U' = U - 2J_H$ based on rotational invariance, and we fix $J_H = U/4$ because this value is widely accepted in iron superconductors to be realistic [28]. For these reasons, only U and λ are free parameters in our study. Future work can analyze in more detail the influence of varying the Hund coupling as well as other parameters in the model.

The SOC term is

$$H_{\text{SOC}} = \lambda \sum_{i,\gamma,\gamma',\sigma,\sigma'} \langle \gamma | \mathbf{L}_i | \gamma' \rangle \cdot \langle \sigma | \mathbf{S}_i | \sigma' \rangle c_{i\sigma\gamma}^\dagger c_{i\sigma'\gamma'}, \quad (3)$$

where λ is the SOC coupling strength, as already explained. Because of the presence of the SOC term the total spin along the z -axis, S_z , is no longer a good quantum number; hence, we cannot target specific S_z sectors in our numerical DMRG calculation. To reduce the computational cost, we have instead selected the parameters contained in H_K such that $[H, J_z^{\text{eff}}] = 0$ where $\mathbf{J}^{\text{eff}} = \sum_i (\mathbf{S}_i + \mathbf{L}_i)$. Note that for arbitrary values of the hopping amplitudes and crystal-fields, J_z^{eff} is also not a good quantum number as discussed in the Appendix A. We then target subspaces with a fixed total $J_z^{\text{eff}} = \sum_i (J_z^{\text{eff}})_i$ for the system. The SOC term is diagonalized in the j^{eff} basis, where j^{eff} is the quantum number associated with \mathbf{J}^{eff} (to avoid complications in the notation, as when j^{eff} should appear as subindex, sometimes this quantum number will be denoted simply by j). m is the projection along the z -axis namely the quantum number of J_z^{eff} . The fact that the good quantum numbers for the SOC term are associated with the effective angular momentum, instead of the total angular momentum ($\mathbf{J} = \mathbf{S} + \mathbf{L}$), is a consequence of the “ t_{2g} - p ” equivalence discussed in [47]. The “ t_{2g} subspace” of the d -orbitals ($l = 2$ for a complete d orbital set) has $\langle \mathbf{L}^2 \rangle = 2$ for a single electron, hence “ t_{2g} ” is isomorphic to the $l = 1$ space (i.e., the p -orbitals) under the following mapping: $|1\rangle_p \equiv -i|-1\rangle_d$, $|-1\rangle_p \equiv i|1\rangle_d$, $|0\rangle_p \equiv |xy\rangle_d$, and $\mathbf{L}^{l=1} \equiv -\mathbf{L}^{t_{2g}}$.

The transformation between the t_{2g} orbitals and the j^{eff} basis is given by (dropping site i index)

$$\begin{bmatrix} a_{\frac{3}{2}, \frac{3}{2}} \\ a_{\frac{3}{2}, -\frac{3}{2}} \\ a_{\frac{1}{2}, -\frac{3}{2}} \end{bmatrix} = \begin{bmatrix} \frac{is}{\sqrt{2}} & \frac{1}{\sqrt{2}} & 0 \\ \frac{s}{\sqrt{6}} & \frac{i}{\sqrt{6}} & \frac{2}{\sqrt{6}} \\ \frac{-s}{\sqrt{3}} & \frac{-i}{\sqrt{3}} & \frac{1}{\sqrt{3}} \end{bmatrix} \begin{bmatrix} c_{\sigma yz} \\ c_{\sigma xz} \\ c_{\sigma xy} \end{bmatrix}, \quad (4)$$

where s is 1(−1) when σ is \uparrow (\downarrow) and $\bar{\sigma} = -\sigma$. The H_{SOC} term in the j^{eff} basis becomes

$$\begin{aligned} H_{\text{SOC}} = \sum_i \frac{\lambda}{2} & (-a_{i, \frac{3}{2}, \frac{3}{2}}^\dagger a_{i, \frac{3}{2}, \frac{3}{2}} - a_{i, \frac{3}{2}, -\frac{3}{2}}^\dagger a_{i, \frac{3}{2}, -\frac{3}{2}} \\ & - a_{i, \frac{3}{2}, -\frac{3}{2}}^\dagger a_{i, \frac{3}{2}, -\frac{3}{2}} - a_{i, \frac{3}{2}, \frac{3}{2}}^\dagger a_{i, \frac{3}{2}, \frac{3}{2}} \\ & + 2a_{i, \frac{1}{2}, \frac{1}{2}}^\dagger a_{i, \frac{1}{2}, \frac{1}{2}} + 2a_{i, \frac{1}{2}, -\frac{1}{2}}^\dagger a_{i, \frac{1}{2}, -\frac{1}{2}}). \end{aligned} \quad (5)$$

The SOC component commutes with $(\mathbf{J}^{\text{eff}})^2$. As a consequence, in the H_{SOC} term there is four(two)-fold degeneracy in the $j^{\text{eff}} = 3/2$ ($1/2$) bands. However, the four-fold degeneracy of the $j^{\text{eff}} = 3/2$ sector breaks into a pair of two-fold Kramer degeneracies due to the presence of the non-cubic t_{2g} -band structure used in our model. This can be understood by analyzing the H_K term in the (j^{eff}, m) basis. In Fig. 1 we show explicitly the connections contained in H_K between the t_{2g} states and the corresponding connections between (j^{eff}, m) states, after imposing the constraints on the hopping and crystal-field parameters (see Appendix A). We have noticed that the non-cubic nature of the t_{2g} states (i.e., the non-degeneracy of the d_{xy} with the $\{d_{xz}, d_{yz}\}$ states, consequence of the tetragonal type t_{2g} bands) leads to hybridization between $(j^{\text{eff}} = 1/2, m = \pm 1/2)$ and $(j^{\text{eff}} = 3/2, m = \pm 1/2)$ states. This hybridization breaks the four-fold degeneracy of the $j^{\text{eff}} = 3/2$ states and also leads to the formation of new bands in which $H_K + H_{\text{SOC}}$ is diagonalized.

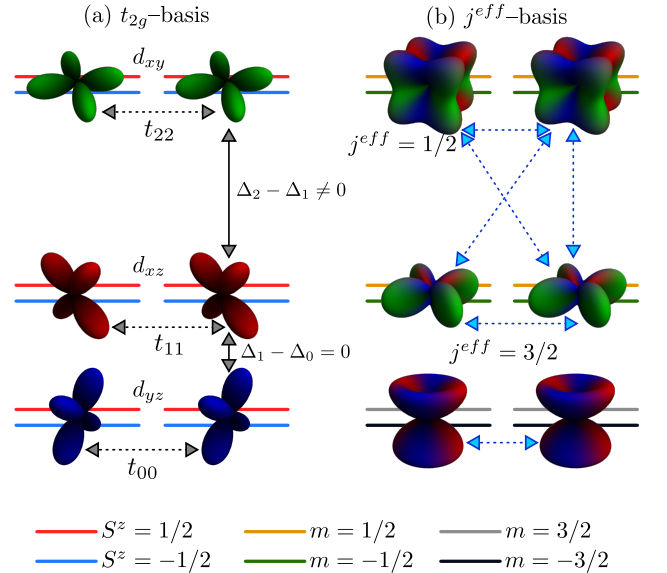


FIG. 1. In panel (a) we show the connections between t_{2g} orbitals using dashed lines, while in panel (b) the dashed lines represent the non-zero connections present in the (j^{eff}, m) basis if we use the proper hopping and crystal-field parameters satisfying the constraints described in the Appendix A.

After using the inverse transformation of Eq. (4) in the tight-binding term, we diagonalized the $H_K + H_{\text{SOC}}$ together to obtain the following bands

$$H_K + H_{\text{SOC}} = \sum_{k,\alpha,s} E_\alpha(k) \tilde{a}_{k,\alpha,s}^\dagger \tilde{a}_{k,\alpha,s}, \quad (6)$$

where $s \in \{1, -1\}$ and $\alpha \in \{0, 1, 2\}$. Here α is the band index, and the relation between $\tilde{a}_{k,\alpha,s}^\dagger$ and $a_{k,j,m}$ is shown in the Appendix B. The dispersion relations for the bands are $E_0(k) = \epsilon_0(k) - \frac{\lambda}{2}$, and $E_\alpha(k) = \frac{1}{2}[\epsilon_2(k) + \epsilon_1(k) + \frac{\lambda}{2} + (-1)^\alpha \sqrt{(\epsilon_2(k) - \epsilon_1(k) - \frac{\lambda}{2})^2 + 2\lambda^2}]$

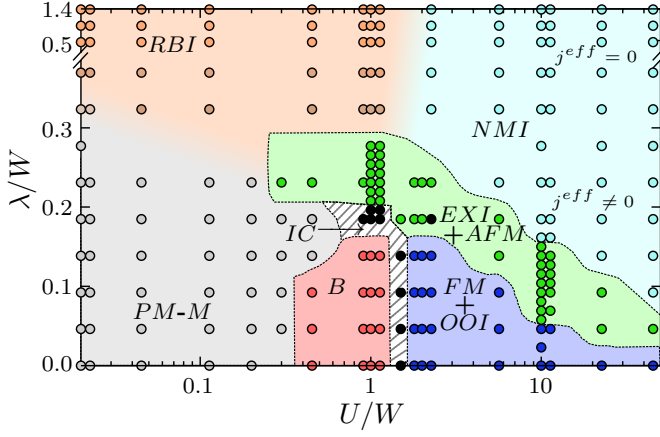


FIG. 2. λ - U phase diagram (note the log scale in U/W -axis). RBI, PM-M, B, FM, OO, IC, EXI, AFM, and NMI stands for relativistic band insulator, paramagnetic metal, block phase, ferromagnetic, orbital ordering, incommensurate, excitonic insulator, antiferromagnetic, and nonmagnetic insulator, respectively. Lines separating phases are guides to the eyes. The actual small circles indicate specific values of data points that were investigated with DMRG. Their high density indicates that this effort has been computationally demanding.

for $\alpha \in \{1, 2\}$; where $\epsilon_\alpha(k) = -2t_{\alpha\alpha} \cos(k) + \Delta_\alpha$ for $\alpha \in \{0, 1, 2\}$. At $\lambda = 0$, the bands 0, 1, and 2 reduce to the standard bands of the d_{yz} , d_{xz} , and d_{xy} orbitals, respectively. For $\lambda/W \gg 0$, the bands 1 and 2 reduce to the $(j^{eff} = 1/2, m = \pm 1/2)$ and $(3/2, \pm 1/2)$ states, respectively, and $n_{3/2, \pm 3/2} = \tilde{n}_{0 \pm 1}$ for any λ . The above described non-interacting portion of the Hamiltonian is useful to understand the effect of spin-orbit coupling in the small U/W region of the phase diagram, as discussed below.

Our many-body calculations are performed using the DMRG technique [48–50] applied to one dimensional chains of various system lengths, such as $L = 8, 16, 24$, and 32 sites. We have used up to 600 states for the DMRG process and have maintained a truncation error

below 10^{-14} throughout the finite algorithm sweeps. In the latter, we performed 10 to 15 full sweeps to gain convergence depending on the system size. We studied the presence of various phases by calculating expectation values of $n_{i\alpha}$, n_{ijm} , \mathbf{S}_i^2 , \mathbf{L}_i^2 , $(\mathbf{J}^{eff})_i^2$, the canonical spin structure factor $S(q)$, and the exciton pair-pair correlation $\langle \Delta_{jm}^{\dagger}(i) \Delta_{jm}(i') \rangle$ (defined in III.B).

III. RESULTS

The main result of this publication, presented in Fig. 2, is the phase diagram of the three-orbital Hubbard model analyzed here, varying U and λ in units of the bandwidth W at a fixed electronic density of four electrons per site on average. In the following subsections, details are provided for the three special cases of weak, intermediate, and strong Hubbard U coupling. Also note that our study is in one dimension and for this reason when we write that at some values of U and λ we are at a phase with some particular characteristics, this has to be interpreted in the sense of dominant power-law decaying correlations as opposed to true long-range order.

A. Paramagnetic Metal and Relativistic Band Insulator (Weak Coupling)

First, we will briefly discuss the small U region, i.e., the weak coupling limit. This regime can be understood by analyzing the non-interacting limit using Eq. (6). Varying the strength of the spin-orbit coupling λ at $U/W = 0$ the exact band structure is shown in Fig. 3(a,b,c). From this analysis we expect the presence of a trivial paramagnetic metal (PM-M) at small λ which transforms into the relativistic band insulator (RBI) regime by increasing λ . At $U = 0$, for four electrons per site, we can use the condition $E_2(k = \pi) = E_1(0)$ to calculate analytically the critical spin-orbit coupling strength λ_c for which a gap opens:

$$\lambda_c(U = 0) = \frac{2t_{11}t_{22}(\Delta_2 - \Delta_1) + 2(t_{11} + t_{22})\sqrt{t_{11}t_{22}(4t_{11}t_{22} + 8(t_{11} + t_{22})^2 - 2(\Delta_2 - \Delta_1)^2)}}{2(t_{11} + t_{22})^2 + t_{11}t_{22}}. \quad (7)$$

The value of λ_c/W for our specific hopping parameters and crystal-field splittings is $\simeq 0.33$. The state $(j^{eff} = 3/2, m = \pm 3/2)$ moves below the Fermi level before λ approaches λ_c as $(j^{eff} = 3/2, m = \pm 3/2)$ does not hybridize with any other state. For the $U \neq 0$ case, but still small, λ_c can be different from $\lambda_c(U = 0)$. We suspect λ_c decreases monotonically as U increases because at intermediate U the excitonic insulator regime develops (see Sec. III.B) for λ lower than $\lambda_c(U = 0)$, and

this Bardeen-Cooper-Schrieffer (BCS) limit of the excitonic insulator (EXI) regime (discussed in next Section) at intermediate U should be present near the semimetal-semiconductor transition as discussed before [51]. The decrease in λ_c is a result of renormalization of bands due to correlation effects, which enhances the effect of spin-orbit coupling, as discussed in [52]. In Fig. 3(d), we show the occupation of the (j^{eff}, m) bands (n_{jm} are the respective densities) varying λ/W at a fixed $U/W = 0.02$,

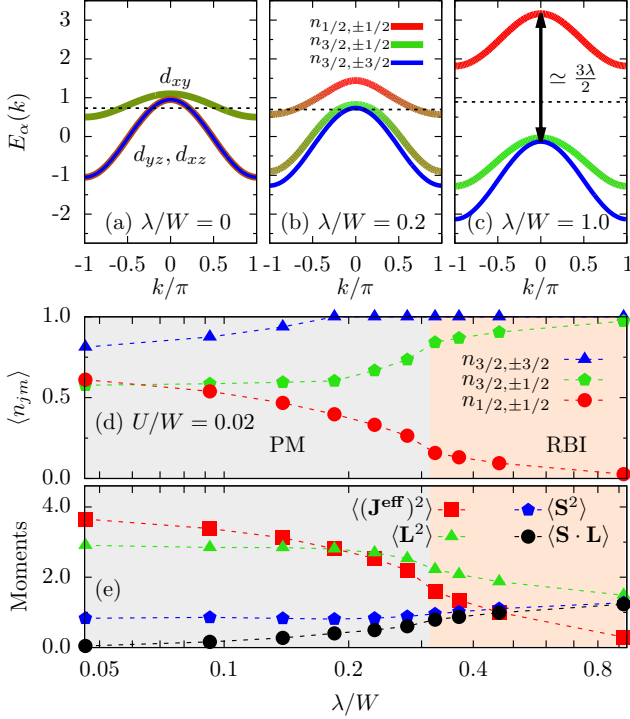


FIG. 3. Panel (a) shows the non-interacting bands of our model at $\lambda/W = 0.0$. As explained in the text, the almost fully populated bands are degenerate and superimposed. In (b) and (c), we show the bands at $\lambda/W = 0.2$ and 1.0 , respectively. Panel (c) displays a clear opening of a gap, i.e., the system becomes a band insulator. Colors are decided depending on the relative contributions from the three (j^{eff}, m) bands, with the pure cases shown in the legend of panel (c). Panel (d) contains the occupation numbers in the (j^{eff}, m) basis, while panel (e) has the local magnetic moments strengths (see legend) as well as $\langle \mathbf{S} \cdot \mathbf{L} \rangle$, all at $U/W = 0.02$. Calculations for panels (d) and (e) were performed with DMRG using a $L = 16$ chain, while panels (a,b,c) are from exact analytical formulas.

displaying a smooth crossover from paramagnetic metal to band insulator. At large λ the $j^{eff} = 3/2$ bands are completely filled, while the $j^{eff}=1/2$ band is nearly empty at $\lambda/W = 1.0$ and its population continues decreasing as λ is further increased.

In contrast to previous DMFT studies performed for three degenerate bands [35, 36], the four-fold degeneracy of the $j^{eff} = 3/2$ bands is here explicitly broken due to the hybridization between the $(3/2, \pm 1/2)$ and $(1/2, \pm 1/2)$ states. This is a consequence of a non-cubic crystal-field splitting and specific hopping parameters to resemble iron-based superconductors, as explained before. We also observed the above mentioned splitting in the intermediate and strong Hubbard coupling limits, thus, this effect propagates into the interacting region. It is important to mention here that due to the hybridization of our model, in the RBI regime the $j^{eff} = 1/2$ state can have a non-zero occupation because it can have non-

zero weight in the band below the Fermi surface. In other words, due to the hybridization between the $(3/2, \pm 1/2)$ and $(1/2, \pm 1/2)$ states, the basis where $H_K + H_{SOC}$ is diagonalized corresponds to $\tilde{a}_{k,\alpha,s}$, not $a_{k,j,m}$. As a consequence, in the lower portion of the RBI region in the phase diagram we have a finite occupation of the $(1/2, \pm 1/2)$ states coexisting with a sharp band insulator gap at the Fermi level. Only as the spin-orbit coupling continues increasing is that $\tilde{a}_{k,\alpha,s}$ reduces asymptotically to $a_{k,j,m}$, and we reach zero occupation of the $(1/2, \pm 1/2)$ states.

Note that a similar splitting between the $j^{eff} = 3/2$, $m = \pm 1/2$ and $j^{eff} = 3/2$, $m = \pm 3/2$ bands of nearly 0.7 eV has also been observed in the $(t_{2g})^5$ perovskite CaIrO_3 [43] as a result of the presence of a non-cubic crystal-field, although our study is not directly related to this material.

Figure 3(e) shows the local moments $\langle (\mathbf{J}^{eff})^2 \rangle$, $\langle \mathbf{L}^2 \rangle$, and $\langle \mathbf{S}^2 \rangle$, as well as $\langle \mathbf{S} \cdot \mathbf{L} \rangle$. Similarly to the non-interacting case, at $U/W = 0.02$, the moments $\langle \mathbf{L}^2 \rangle$, $\langle \mathbf{S}^2 \rangle$, and $\langle \mathbf{S} \cdot \mathbf{L} \rangle$ converge to $4/3$ while $\langle (\mathbf{J}^{eff})^2 \rangle$ tends to 0 for large spin-orbit coupling (this can be checked by using the atomic state $a_{\frac{3}{2},\frac{3}{2}}^\dagger a_{\frac{3}{2},-\frac{3}{2}}^\dagger a_{\frac{3}{2},\frac{1}{2}}^\dagger a_{\frac{3}{2},-\frac{1}{2}}^\dagger |0\rangle$, which is the ground state of the H_{SOC} term).

B. Excitonic Insulator and Orbital Selective Mott Phase (Intermediate Coupling)

In this subsection we will discuss the results obtained at intermediate Hubbard interaction. This region is difficult and it cannot be treated perturbatively, thus numerical exact studies via the DMRG method are important. In this regime we have found several interesting phases such as the OSMF, EXI, incommensurate phase, and at large λ/W we again found the RBI of weak coupling. In Fig. 4, we present results obtained at $U/W = 1.0$. At small λ , we reproduced the OSMF regime with a magnetic Block arrangement of the spins ($\uparrow\uparrow\downarrow\downarrow\uparrow\uparrow$) [31–34]. The presence of OSMF features is confirmed by measuring the occupation of the t_{2g} states: in this regime the d_{xy} orbital has occupation very close to 1, while $d_{xz}(y_z)$ has occupation nearly 1.5 (see Appendix C). The spin structure factor $S(q)$ and the real-space spin-spin correlations are shown in Fig. 5(a,c) at $\lambda/W = 0.046$ providing evidence for the Block magnetic order.

Figure 4(a) shows the occupation number in the (j^{eff}, m) states corresponding to $U/W = 1.0$ at different λ 's. As in the case of weak coupling, here the system also converges to a band insulator at sufficiently large spin-orbit coupling as the $j^{eff} = 3/2$ state is completely filled and $j^{eff} = 1/2$ becomes empty. In the strength of the magnetic moments we have noticed a clear difference between the intermediate and weak coupling regimes, as shown Fig. 4(c). We found $\langle \mathbf{S}^2 \rangle = 2$ in the OSMF and in the incommensurate phase. However, this quantity is reduced after entering in the EXI phase, and at the same time $\langle \mathbf{L}^2 \rangle$ increases. We also

noticed that for any Hubbard interaction in the limit of sufficiently large λ , $\langle \mathbf{S}^2 \rangle = \langle \mathbf{L}^2 \rangle = \langle \mathbf{S} \cdot \mathbf{L} \rangle$ which means \mathbf{S} and \mathbf{L} become parallel to each other. As a consequence, $\langle (\mathbf{J}^{eff})^2 \rangle = \langle \mathbf{S}^2 \rangle + \langle \mathbf{L}^2 \rangle - 2\langle \mathbf{S} \cdot \mathbf{L} \rangle$ converges to 0.

To identify the EXI phase, we calculated a pair-pair correlation function (note, here “pair” denotes an *electron-hole* pair), i.e., $\langle \Delta_{jm}^{\dagger \tilde{j}m}(i) \Delta_{jm}^{\tilde{j}m}(i') \rangle$, where $\Delta_{jm}^{\tilde{j}m}(i) = a_{i\tilde{j}m}^\dagger a_{ijm}$ (here we fixed $j = 1/2$ and $\tilde{j} = 3/2$). This operator was already introduced in previous literature [35, 36]. In our DMRG calculations, and in agreement with [35], we noticed that in the EXI phase the correlation $\langle \Delta_{jm}^{\dagger \tilde{j}m}(i) \Delta_{jm}^{\tilde{j}m}(i') \rangle$ develops staggered ordering, justifying the staggered sign used below. In Fig. 4(b), we show the associated correlations summed over all distances (with $j = 1/2$ and $\tilde{j} = 3/2$),

$$\Delta_m = \frac{1}{L^2} \sum_{|i-i'|>0} (-1)^{|i-i'|} \langle \Delta_{jm}^{\dagger \tilde{j}m}(i) \Delta_{jm}^{\tilde{j}m}(i') \rangle. \quad (8)$$

Then Δ_m is a measure of the staggered pair-pair correlations associated with the EXI state.

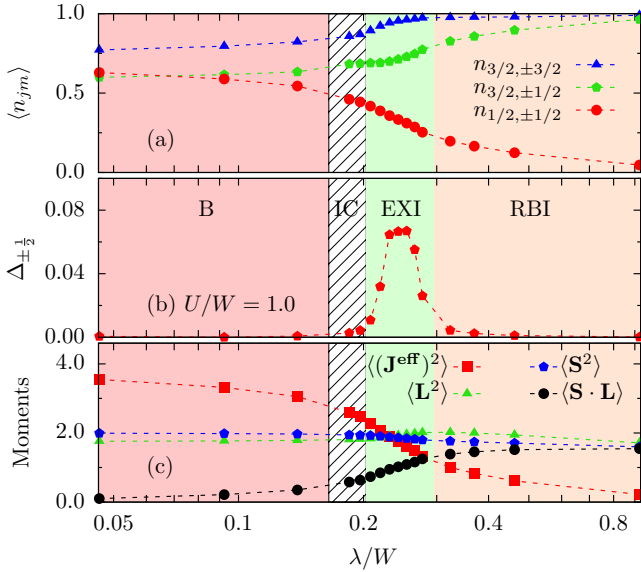


FIG. 4. DMRG results obtained at $U/W = 1$ (intermediate coupling) and using a $L = 16$ system. Panel (a) shows occupation number in the (j^{eff}, m) bands while (b) shows the excitonic parameter Δ_m defined in Eq.(8) varying λ/W . Panel (c) shows the three local moment strengths as well as $\langle \mathbf{S} \cdot \mathbf{L} \rangle$.

Intuitively, in the EXI phase we have hole-electron pairs involving the $(j^{eff} = 3/2, \pm 1/2)$ and $(1/2, \pm 1/2)$ manifolds. In the absence of direct hopping between the bands, there is a conservation of the number of electrons in each band. A nonzero expectation value for $\Delta_{jm}^{\tilde{j}m}(i)$ (which becomes an order parameter for this case) amounts to a spontaneous symmetry breaking of the $U(1)$ symmetry that corresponds to the relative phase

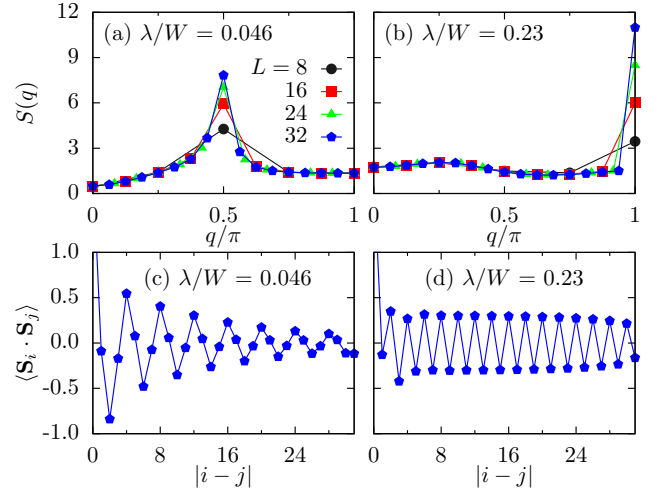


FIG. 5. DMRG results obtained at $U/W = 1$. Panels (a) and (b) contain the spin structure factor in the block phase and in the EXI phase, respectively, for various number of sites $L = 8$ (black), 16 (red), 24 (green), and 32 (blue). Panels (c) and (d) display the real-space spin-correlations at $L = 32$ corresponding to the block and EXI phases, respectively, for the λ/W 's indicated.

of the bands in which the electron-hole pair forms [53]. However, because we are using non-cubic bands with a crystal-field splitting, this symmetry is explicitly broken in our Hamiltonian, namely in the tight-binding term transformed to the “ a ” basis there is a direct hopping between the $(3/2, \pm 1/2)$ and $(1/2, \pm 1/2)$ bands. Thus, it is somewhat surprising that the expectation values used in our work (like Δ_m) still behave in practice similarly as the true order parameter used in [35, 36], namely it is robust in the EXI phase and very small in other phases [see Fig. 4(b)].

We also found that the staggered excitonic condensate is always present in combination with AFM spin ordering, as deduced from the spin structure factor $S(q)$ and the real-space spin-spin correlations presented in Fig. 5(b,d) at $\lambda/W = 0.23$. We also carried out finite-size scaling of $S(q)$ for system sizes $L = 8, 16, 24$, and 32 at $\lambda/W = 0.046$ and 0.23. We noticed a fast growth in the peak value at $q = \pi$ for $\lambda/W = 0.23$, indicating that spin antiferromagnetism and excitonic order are linked together. This aspect of stabilizing antiferromagnetism in an EXI phase due to robust Hund’s coupling, as used by us, was discussed before in [54]. Exploring the effects of varying the Hund’s coupling in our model can be carried out in future work.

C. Strong Coupling

Consider now the large U/W limit. In Fig. 6(a-e) we present some results obtained at $U/W = 10$. At small λ/W , we found a robust ferromagnetic (FM) spin order as shown in Fig. 6(d) via the spin structure fac-

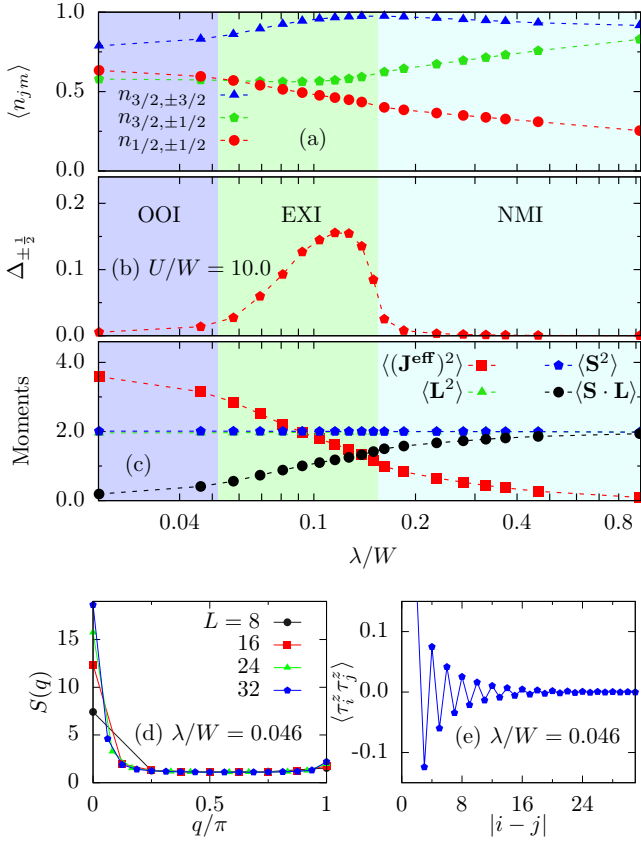


FIG. 6. DMRG results obtained at $U/W = 10$ (strong coupling regime). Panel (a) shows the occupation number in the (j^{eff}, m) bands, while panel (b) displays the excitonic order parameter dependence on λ/W . Panel (c) displays the local moment strengths and also $\langle \mathbf{S} \cdot \mathbf{L} \rangle$. Panel (d) contains the spin structure factor for a number of sites L equal to 8 (black), 16 (red), 24 (green), and 32 (blue). Panel (e) shows $\langle \tau_z(i)\tau_z(j) \rangle$ for $L=32$. Both (d) and (e) are in the ferromagnetic and orbitally ordered phase at $\lambda/W = 0.046$.

tor. We also noticed that this FM spin ordering is always accompanied by orbital ordering, as discussed in previous investigations in the absence of spin-orbit coupling [34]. To clarify the nature of the orbital order, we show $\langle \tau_z(i)\tau_z(j) \rangle$ in Fig. 6(e), where $\tau_z(i) = n_{iyz} - n_{ixz}$ is the z component of the pseudospin operator in orbital space. This orbital ordering leads to the opening of a gap in the system rendering the state an orbital-ordered insulator (OOI), as discussed in [34] via determinant Quantum Monte Carlo and DMRG calculations without spin-orbit coupling.

By increasing λ/W , we have observed a transition from FM to the AFM spin ordering shown in Fig. 7(a,b). As in Sec. III.B, this AFM ordering is accompanied by staggering in the exciton pair-pair correlation as shown in Fig. 7(c,d). Similar phases were noticed in a study of the low-energy effective Hamiltonian for the $(t_{2g})^4$ sector in [24]. Note that at $U/W = 10$ the excitonic condensate starts at smaller λ/W than those needed at intermediate value of U/W [Fig. 6(b)]. Interestingly, in the EXI phase

we have noticed that $\langle n_{3/2,\pm 3/2} \rangle$ converges to ≈ 1 (to be precise 0.98) and then reverses the trend and starts decreasing in the region identified as a non-magnetic insulator (see below). This is different from the properties of the EXI phase observed at intermediate U/W where $\langle n_{3/2,\pm 3/2} \rangle < 1$ and then slowly converged to 1 as the system evolves to become a band insulator increasing λ/W further.

At $U/W=10$, and at any λ/W , we also noticed that $\langle \mathbf{S}^2 \rangle = 2$ and $\langle \mathbf{L}^2 \rangle = 2$ [Fig. 6(c)]. These vector operators become parallel only for large λ/W , namely where $\langle \mathbf{S} \cdot \mathbf{L} \rangle = 2$ and $\langle (\mathbf{J}^{eff})^2 \rangle = 0$. In Fig. 7(d) we show the pair-pair excitonic correlation as a function of distance, involving the operator $\Delta_{j,m}^{\dagger}(i) = a_{ijm}^{\dagger} a_{ijm}$. In all points studied inside the EXI phase we observed a staggering in the pair-pair correlation. In Fig. 7(c), we show $\Delta_m(q) = \frac{1}{L} \sum_{i,j} e^{q(i-j)} \langle \Delta_{jm}^{\dagger}(i) \Delta_{jm}(j) \rangle$ for various λ 's at strong U , where q is the momentum.

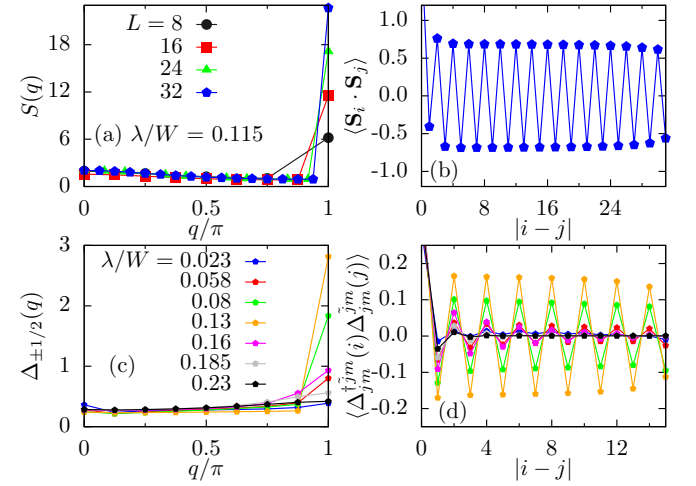


FIG. 7. DMRG results obtained at $U/W=10$. Panel (a) depicts the spin structure factor in the EXI phase at $\lambda/W=0.115$, for a number of sites L equal to 8 (black), 16 (red), 24 (green), and 32 (blue). Panel (b) shows the real-space averaged spin-spin correlations for $\lambda/W=0.115$. In (c) and (d), we present the pair-pair correlation in momentum and real space, respectively, for a $L = 16$ system. In panel (d) $j = 1/2$, $\tilde{j} = 3/2$, and $m = \pm 1/2$ were used.

In Fig. 8 we present $\langle n_l^2 \rangle - \langle n_l \rangle^2 = \frac{1}{L} \sum_i \langle n_{i,l}^2 \rangle - \langle n_{i,l} \rangle^2$, where the index l takes the values indicated in the legend of panel (a), namely $j^{eff} = 1/2$, $(j^{eff}, |m|) = (3/2, 1/2)$, $(j^{eff}, |m|) = (3/2, 3/2)$, and $Total$ ($n_{Total} = \sum_{i,j,m} n_{ijm}$). Interestingly, we noticed that in the EXI phase the charge fluctuations increase for $j^{eff} = 1/2$ and $(j^{eff}, |m|) = (3/2, 1/2)$: these are the bands where excitons are located, and this feature is common for both intermediate and strong coupling EXI regimes. However, we have identified some differences within the EXI region between the intermediate and strong Hubbard coupling regions. In strong coupling [Fig. 8(c)] we noticed that in the EXI regime the local charge fluctuations per site

are nearly zero, suggesting that electrons are almost localized. However, at intermediate coupling [$U/W = 1$, Fig. 8(b)] and still within the EXI regime, the total charge fluctuations are nonzero. Nonzero local charge fluctuations in the EXI phase hints towards exciton pairs that are extended in size, namely the BCS type limit of excitonic phases. In the other extreme, namely the Bose-Einstein condensation (BEC) limit, the excitonic phase should have small charge fluctuations because the exciton pairs are considerably smaller and of atomic-scale size. A more detailed study of the BCS-BEC crossover within the excitonic phase when moving from intermediate to strong coupling U/W is currently in progress.

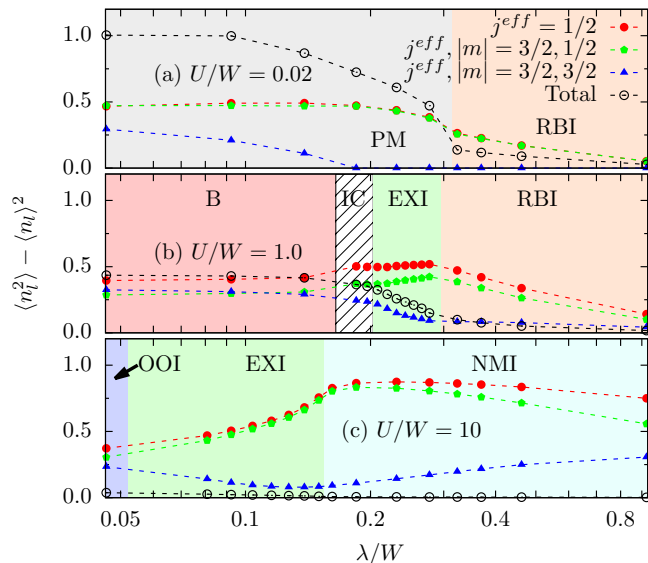


FIG. 8. Averaged local charge fluctuations of the (j^{eff}, m) states (as indicated in the upper panel legend) corresponding to (a) $U/W = 0.02$ (weak coupling), (b) $U/W = 1$ (intermediate coupling), and (c) $U/W = 10$ (strong coupling).

In the strong coupling region of focus here and in the neighborhood of the EXI phase we have found a non-magnetic insulator (NMI) with $\langle (\mathbf{J}^{eff})^2 \rangle \neq 0$. Let us contrast the NMI and RBI regions. To identify the NMI regime we focused on two aspects: (i) the system should have localized electrons due to strong correlations; (ii) there is no magnetic ordering. The first condition was checked by calculating local charge fluctuations, as shown in Fig. 8, where we observed that the local charge fluctuations are zero throughout this region [Fig. 8(c)]. This is merely a strong correlation effect different from the case of the small U/W and large λ/W regime (RBI) where electrons are primarily in extended states but still having zero local charge fluctuations because of having nearly full and empty bands. As depicted in Fig. 8(a,b), in the RBI region the local charge fluctuations separately in each (j^{eff}, m) state as well as *Total* are small or nearly zero. On the other hand, in the NMI region only *Total* is zero but charge fluctuations separately for each (j^{eff}, m) are large [shown in Fig. 8(c)]. This suggests that in the

case of NMI the electrons are not locked just as the consequence of having a fully filled band or an empty band like in RBI, but as a consequence of strong correlations.

In recent work using DMFT [36] for a cubic $(t_{2g})^4$ system, a $\langle (\mathbf{J}^{eff})^2 \rangle = 0$ NMI state was also found in the vicinity of the excitonic condensate and it was identified as a Van Vleck-type Mott insulator, as discussed earlier in [55]. Our finding of a NMI state with $\langle (\mathbf{J}^{eff})^2 \rangle \neq 0$ near the excitonic condensate seems in contrast with those previous studies, but it is merely a consequence of using a non-cubic band structure. Interestingly, this breakdown of the $\langle (\mathbf{J}^{eff})^2 \rangle = 0$ state was also recently noticed in first-principle calculations [18, 56] applied to the $(t_{2g})^4$ iridate Sr_2YIrO_6 . In our results, and to the best of our accuracy, the $\langle (\mathbf{J}^{eff})^2 \rangle \neq 0$ NMI region is smoothly connected to the $\langle (\mathbf{J}^{eff})^2 \rangle = 0$ region.

IV. CONCLUSIONS

In this publication, using an accurate computational technique we have studied the phase diagram of an electronic model simultaneously with Hubbard, Hund, and spin-orbit couplings. The hopping amplitudes were fixed to those used in a previous study at $\lambda = 0$, since that effort already unveiled a variety of interesting phases such as the OSMF regime. In the present analysis our main result is shown in Fig. 2. The previously identified Block and FM-OO phases were followed increasing λ . Eventually, over a broad range of U/W an excitonic condensate phase was identified, in qualitative agreement with previous DMFT studies. The large λ regime is also interesting, with a variety of insulating regions.

Conceptually, our analysis provides an avenue to study quasi-one dimensional materials with robust spin-orbit coupling. We provide a tentative partial list of materials of this class in the introduction and throughout the text. In combination with *ab-initio* techniques, needed for the hopping amplitudes, our many-body procedure can unveil properties of these systems in reduced dimensionality with good precision to guide experiments. We hope our work triggers the cross-fertilization between theory and experiments needed to develop the novel field of quasi-one dimensional iridates, or other related low-dimensional materials with robust spin-orbit coupling.

V. ACKNOWLEDGMENTS

The authors acknowledge useful conversations with Prof. G. Cao. N.K. was supported by the National Science Foundation Grant No. DMR-1404375. J.H, A.N., A.M., F.R., and E.D. were supported by the US Department of Energy (DOE), Office of Basic Energy Sciences (BES), Materials Sciences and Engineering Division. The work of G.A. was conducted at the Center for Nanophase Materials Science, sponsored by the Scientific User Fa-

cilities Division, BES, DOE, under contract with UT-Battelle.

Appendix A: Theorem for conservation of J_z^{eff}

As discussed in Sec. II, to reduce the computational cost of our numerical calculations we target specific J_z^{eff} sectors. In order for J_z^{eff} to become a good quantum

number, namely to achieve $[H, J_z^{eff}] = 0$, we need to choose carefully the parameters contained in H_K (both the crystal-field splittings and hopping parameters) so that they satisfy the constraints discussed in this Appendix.

Below in Eq. (A1) we show H_K explicitly written in the a_{jm} basis. This is calculated simply by using the inverse transformation of Eq. (4).

$$\begin{aligned}
 H = \sum_{\langle ll' \rangle} & \begin{bmatrix} a_{l, \frac{3}{2}, \frac{3}{2}}^\dagger & a_{l, \frac{3}{2}, -\frac{1}{2}}^\dagger & a_{l, \frac{1}{2}, -\frac{1}{2}}^\dagger & a_{l, \frac{3}{2}, -\frac{3}{2}}^\dagger & a_{l, \frac{3}{2}, \frac{1}{2}}^\dagger & a_{l, \frac{1}{2}, \frac{1}{2}}^\dagger \\ \frac{t_{00}+t_{11}}{2} & \frac{it_{00}-it_{11}+2t_{01}}{2\sqrt{3}} & \frac{-it_{00}+it_{11}-2t_{01}}{\sqrt{6}} & 0 & \frac{t_{12}+it_{02}}{\sqrt{3}} & \frac{t_{12}+it_{02}}{\sqrt{6}} \\ \frac{-it_{00}+it_{11}+2t_{01}}{2\sqrt{3}} & \frac{t_{00}+t_{11}+4t_{22}}{6} & \frac{-t_{00}-t_{11}+2t_{22}}{3\sqrt{2}} & \frac{t_{12}+it_{02}}{\sqrt{3}} & 0 & \frac{t_{02}+it_{12}}{\sqrt{2}} \\ \frac{it_{00}-it_{11}-2t_{01}}{\sqrt{6}} & \frac{-t_{00}-t_{11}+2t_{22}}{3\sqrt{2}} & \frac{t_{00}+t_{11}+t_{22}}{3} & \frac{t_{12}+it_{02}}{\sqrt{6}} & \frac{-t_{02}-it_{12}}{\sqrt{2}} & 0 \\ 0 & \frac{t_{12}-it_{02}}{\sqrt{3}} & \frac{t_{12}-it_{02}}{\sqrt{6}} & \frac{t_{00}+t_{11}}{2} & \frac{it_{00}-it_{11}+2t_{01}}{2\sqrt{3}} & \frac{-it_{00}+it_{11}-2t_{01}}{\sqrt{6}} \\ \frac{t_{12}-it_{02}}{\sqrt{3}} & 0 & \frac{-t_{02}-it_{12}}{\sqrt{2}} & \frac{-it_{00}+it_{11}+2t_{01}}{2\sqrt{3}} & \frac{t_{00}+t_{11}+4t_{22}}{6} & \frac{-t_{00}-t_{11}+2t_{22}}{3\sqrt{2}} \\ \frac{t_{12}-it_{02}}{\sqrt{6}} & \frac{t_{02}-it_{12}}{\sqrt{2}} & 0 & \frac{it_{00}-it_{11}-2t_{01}}{\sqrt{6}} & \frac{-t_{00}-t_{11}+2t_{22}}{3\sqrt{2}} & \frac{t_{00}+t_{11}+t_{22}}{3} \end{bmatrix} \begin{bmatrix} a_{l', \frac{3}{2}, \frac{3}{2}} \\ a_{l', \frac{3}{2}, -\frac{1}{2}} \\ a_{l', \frac{1}{2}, -\frac{1}{2}} \\ a_{l', \frac{3}{2}, -\frac{3}{2}} \\ a_{l', \frac{3}{2}, \frac{1}{2}} \\ a_{l', \frac{1}{2}, \frac{1}{2}} \end{bmatrix} \\
 + \sum_l & \begin{bmatrix} a_{l, \frac{3}{2}, \frac{3}{2}}^\dagger & a_{l, \frac{3}{2}, -\frac{1}{2}}^\dagger & a_{l, \frac{1}{2}, -\frac{1}{2}}^\dagger & a_{l, \frac{3}{2}, -\frac{3}{2}}^\dagger & a_{l, \frac{3}{2}, \frac{1}{2}}^\dagger & a_{l, \frac{1}{2}, \frac{1}{2}}^\dagger \\ \frac{\Delta_0+\Delta_1}{2} & \frac{i\Delta_0-i\Delta_1}{2\sqrt{3}} & \frac{-i\Delta_0+i\Delta_1}{\sqrt{6}} & 0 & 0 & 0 \\ \frac{-i\Delta_0+i\Delta_1}{2\sqrt{3}} & \frac{\Delta_0+\Delta_1+4\Delta_2}{6} & \frac{-\Delta_0-\Delta_1+2\Delta_2}{3\sqrt{2}} & 0 & 0 & 0 \\ \frac{i\Delta_0-i\Delta_1}{\sqrt{6}} & \frac{-\Delta_0-\Delta_1+2\Delta_2}{3\sqrt{2}} & \frac{\Delta_0+\Delta_1+\Delta_2}{3} & 0 & 0 & 0 \\ 0 & 0 & 0 & \frac{\Delta_0+\Delta_1}{2} & \frac{i\Delta_0-i\Delta_1}{2\sqrt{3}} & \frac{-i\Delta_0+i\Delta_1}{\sqrt{6}} \\ 0 & 0 & 0 & \frac{-i\Delta_0+i\Delta_1}{2\sqrt{3}} & \frac{\Delta_0+\Delta_1+4\Delta_2}{6} & \frac{-\Delta_0-\Delta_1+2\Delta_2}{3\sqrt{2}} \\ 0 & 0 & 0 & \frac{i\Delta_0-i\Delta_1}{\sqrt{6}} & \frac{-\Delta_0-\Delta_1+2\Delta_2}{3\sqrt{2}} & \frac{\Delta_0+\Delta_1+\Delta_2}{3} \end{bmatrix} \begin{bmatrix} a_{l, \frac{3}{2}, \frac{3}{2}} \\ a_{l, \frac{3}{2}, -\frac{1}{2}} \\ a_{l, \frac{1}{2}, -\frac{1}{2}} \\ a_{l, \frac{3}{2}, -\frac{3}{2}} \\ a_{l, \frac{3}{2}, \frac{1}{2}} \\ a_{l, \frac{1}{2}, \frac{1}{2}} \end{bmatrix}. \quad (A1)
 \end{aligned}$$

The J_z^{eff} operator can also be written in the same basis as

$$J_z^{eff} = \sum_{ijm} (m) n_{i,j,m}. \quad (A2)$$

Below are the constraints on the H_K parameters (assuming that the $t_{\gamma\gamma'}$ and Δ_γ are real) which are obtained after imposing explicitly the condition $[H_K, J_z^{eff}] = 0$:

- $t_{\gamma\gamma'} = 0 \forall \gamma \neq \gamma'$, i.e., no interorbital hopping,
- $t_{00} = t_{11}$, namely the hopping amplitudes of the d_{xz} and d_{yz} orbitals must be equal,
- $\Delta_0 = \Delta_1$, namely the crystal-field splittings for the d_{xz} and d_{yz} orbitals must be equal.

We have selected the parameters in H_K such that the above constraints are satisfied. These constraints forbid all scattering processes of electrons under which J_z^{eff} changes, but the hybridization between the states ($j_z^{eff} =$

$3/2, m = \pm 1/2$) and ($j_z^{eff} = 1/2, m = \pm 1/2$) is still allowed and our choice of parameters hybridize the above mentioned bands. For this reason $[(J_z^{eff})^2, H_K] \neq 0$.

Appendix B: “Good Basis” for $H_K + H_{SOC}$

In principle we can write the basis in which $H_K + H_{SOC}$ are diagonalized simultaneously. We name these new basis operators as $\tilde{a}_{k,\alpha,s}$; where k is the momentum, α is the band index, and s is the flavour of the particle, i.e., ± 1 . Below is the relation between these new basis and $a_{k,j,m}$, where $a_{k,j,m} = (1/\sqrt{L}) \sum_l e^{ilk} a_{l,j,m}$:

$$\tilde{a}_{k,0,s}^\dagger = a_{k, \frac{3}{2}, \frac{3s}{2}}^\dagger, \quad (B1)$$

$$\tilde{a}_{k,1,s}^\dagger = \frac{1}{N_2(k)} a_{k, \frac{3}{2}, \frac{s}{2}}^\dagger + \frac{1}{N_1(k)} a_{k, \frac{1}{2}, \frac{s}{2}}^\dagger, \quad (B2)$$

$$\tilde{a}_{k,2,s}^\dagger = \frac{(\epsilon_{21}(k) - 9\lambda/2) + 3\sqrt{(\epsilon_{21} - \lambda/2)^2 + 2\lambda^2}}{2\sqrt{2}\epsilon_{21}(k)N_2(k)} a_{k,\frac{3}{2},\frac{s}{2}}^\dagger + \frac{(\epsilon_{21}(k) - 9\lambda/2) - 3\sqrt{(\epsilon_{21} - \lambda/2)^2 + 2\lambda^2}}{2\sqrt{2}\epsilon_{21}(k)N_1(k)} a_{k,\frac{1}{2},\frac{s}{2}}^\dagger, \quad (\text{B3})$$

$$N_\alpha(k) = \frac{3((\epsilon_{21}(k) - \lambda/2)^2 + 2\lambda^2)^{1/4}(\sqrt{(\epsilon_{21}(k) - \lambda/2)^2 + 2\lambda^2} + (-1)^\alpha(\epsilon_{21}(k)/3 - 3\lambda/2))^{1/2}}{2\epsilon_{21}(k)},$$

where in the equations above, $\epsilon_{21}(k) = \epsilon_2(k) - \epsilon_1(k)$.

Using these relations, we calculated the bands for the non-interacting case and the $\lambda_c(U=0)$ for metal-insulator transition, as discussed in Sec. III A.

Appendix C: OSMF in the intermediate and strong U coupling limit

As discussed earlier we found the OSMF in the intermediate and strong coupling regions at small λ , by calculating occupation densities in the t_{2g} basis. In the OSMF region the d_{xy} orbital is filled with nearly one electron per site while $d_{xz(yz)}$ have nearly 1.5 filling. As shown in Fig. 9, we noticed that the EXI regime starts appearing at relatively lower values of λ in the strong U coupling region.

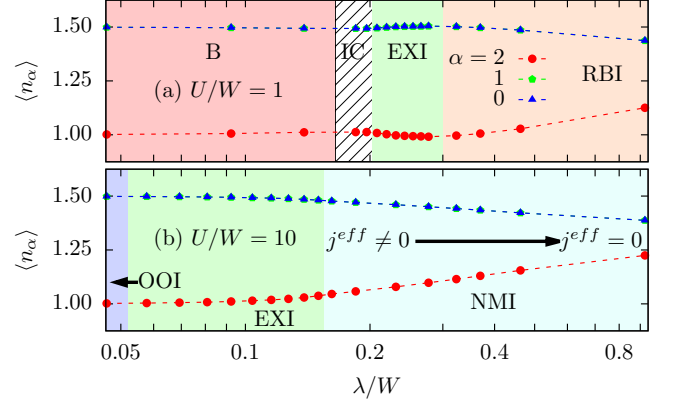


FIG. 9. Occupations of the t_{2g} orbital states corresponding to (a) $U/W = 1$ (intermediate coupling) and (b) $U/W = 10$ (strong coupling). To a good approximation, the excitonic condensate phase behaves similarly as the Block (OSMF) phase, namely with one orbital having occupation of approximately one electron.

- ¹ R. J. Cava, B. Batlogg, K. Kiyono, H. Takagi, J. J. Krajewski, W. F. Peck, Jr., L. W. Rupp, Jr., and C. H. Chen, *Phys. Rev. B* **49**, 11890 (1994).
- ² T. Shimura, Y. Inaguma, T. Nakamura, M. Itoh, and Y. Morii, *Phys. Rev. B* **52**, 9143 (1995).
- ³ G. Cao, J. Bolivar, S. McCall, J. E. Crow, and R. P. Guertin, *Phys. Rev. B* **57**, R11039 (1998).
- ⁴ H. Okabe, M. Isobe, E. Takayama-Muromachi, A. Koda, S. Takeshita, M. Hiraishi, M. Miyazaki, R. Kadono, Y. Miyake, and J. Akimitsu, *Phys. Rev. B* **83**, 155118 (2011).
- ⁵ W. Witczak-Krempa, G. Chen, Y. B. Kim, and L. Balents, *Annu. Rev. Condens. Matter Phys.* **5**, 57 (2014).
- ⁶ H. Watanabe, T. Shirakawa, and S. Yunoki, *Phys. Rev. B* **89**, 165115 (2014).
- ⁷ J. G. Rau, E. K. Lee, and H. Kee, *Annual Review of Condensed Matter Physics* Vol. **7**: 195-221 (2016).
- ⁸ D. Haskel, G. Fabbri, M. Zhernenkov, P. P. Kong, C. Q. Jin, G. Cao, and M. van Veenendaal, *Phys. Rev. Lett.* **109**, 027204 (2012).
- ⁹ G. Cao, and P. Schlottmann, *arXiv:1704.06007*.
- ¹⁰ B. J. Kim, H. Jin, S. J. Moon, J.-Y. Kim, B.-G. Park, C.S. Leem, J. Yu, T. W. Noh, C. Kim, S.-J. Oh, J.-H. Park, V. Durairaj, G. Cao, and E. Rotenberg, *Phys. Rev. Lett.* **101**, 076402 (2008).
- ¹¹ J. Matsuno, Y. Okimoto, Z. Fang, X. Z. Yu, Y. Matsui, N. Nagaosa, M. Kawasaki, and Y. Tokura, *Phys. Rev. Lett.* **93**, 167202 (2004).
- ¹² B. J. Kim, J. Yu, H. Koh, I. Nagai, S. I. Ikeda, S.-J. Oh, and C. Kim, *Phys. Rev. Lett.* **97**, 106401 (2006).
- ¹³ B. J. Kim, H. Ohsumi, T. Komesu, S. Sakai, T. Morita, H. Takagi, and T. Arima, *Science* **323**, 1329 (2009).
- ¹⁴ S. Fujiyama, H. Ohsumi, T. Komesu, J. Matsuno, B. J. Kim, M. Takata, T. Arima, and H. Takagi, *Phys. Rev. Lett.* **108**, 247212 (2012).
- ¹⁵ G. Jackeli and G. Khaliullin, *Phys. Rev. Lett.* **102**, 017205 (2009).
- ¹⁶ H. Watanabe, T. Shirakawa, and S. Yunoki, *Phys. Rev. Lett.* **105**, 216410 (2010).
- ¹⁷ C. Martins, M. Aichhorn, L. Vaugier, and S. Biermann, *Phys. Rev. Lett.* **107**, 266404 (2011).
- ¹⁸ B. F. Phelan, E. M. Seibel, D. B. Jr., W. Xie, and R. Cava, *Solid State Communications* **236**, 37 (2016).
- ¹⁹ G. Cao, T.F. Qi, L. Li, J. Terzic, S.J. Yuan, L.E. DeLong, G. Murthy, and R.K. Kaul, *Phys. Rev. Lett.* **112**, 056402 (2014).
- ²⁰ L. T. Corredor, G. Aslan-Cansever, M. Sturza, Kaustuv Manna, A. Maljuk, S. Gass, T. Dey, A. U. B. Wolter, Olga Kataeva, A. Zimmermann, M. Geyer, C. G. F. Blum, S. Wurmehl, and B. Büchner, *Phys. Rev. B* **95**, 064418 (2017).
- ²¹ J. Terzic, H. Zheng, Feng Ye, H. D. Zhao, P. Schlottmann, L. De Long, and G. Cao, *arXiv:1608.07624v3*.
- ²² T. Dey, A. Maljuk, D. V. Efremov, O. Kataeva, S. Gass, C. G. F. Blum, F. Steckel, D. Gruner, T. Ritschel, A. U. B.

- Wolter, J. Geck, C. Hess, K. Koepernik, J. van den Brink, S. Wurmehl, and B. Bchner, *Phys. Rev. B* **93**, 014434 (2016).
- ²³ O. N. Meetei, W. S. Cole, M. Randeria, and N. Trivedi, *Phys. Rev. B* **91**, 054412 (2015).
- ²⁴ C. Svoboda, M. Randeria, and N. Trivedi, *Phys. Rev. B* **95**, 014409 (2017).
- ²⁵ D. C. Johnston, *Adv. Phys.* **59**, 803 (2010).
- ²⁶ P. J. Hirschfeld, M. M. Korshunov, and I. I. Mazin, *Rep. Prog. Phys.* **74**, 124508 (2011).
- ²⁷ D. J. Scalapino, *Rev. Mod. Phys.* **84**, 1383 (2012).
- ²⁸ P. C. Dai, J. P. Hu, and E. Dagotto, *Nature Phys.* **8**, 709 (2012), and references therein.
- ²⁹ D. Liu, W. Zhang, D. Mou, J. He, Y. Ou, Q. Wang, Z. Li, L. Wang, L. Zhao, S. He *et al.*, *Nature Communications* **3**, 931 (2012).
- ³⁰ S. V. Borisenko, D. V. Evtushinsky, Z.-H. Liu, I. Morozov, R. Kappenberger, S. Wurmehl, B. Bchner, A. N. Yaresko, T. K. Kim, M. Hoesch, T. Wolf and N. D. Zhigadlo, *Nature Physics* **12**, 311 (2016).
- ³¹ J. Rincón, A. Moreo, G. Alvarez, and E. Dagotto, *Phys. Rev. Lett.* **112**, 106405 (2014).
- ³² J. Rincón, A. Moreo, G. Alvarez, and E. Dagotto, *Phys. Rev. B* **90**, 241105(R) (2014).
- ³³ G. Liu, N. Kaushal, S. Li, C. B. Bishop, Y. Wang, S. Johnston, G. Alvarez, A. Moreo, E. Dagotto, *Phys. Rev. E* **93**, 063313 (2016).
- ³⁴ S. Li, N. Kaushal, Y. Wang, Y. Tang, G. Alvarez, A. Nocera, T. A. Maier, E. Dagotto, and S. Johnston, *Phys. Rev. B* **94**, 235126 (2016).
- ³⁵ T. Sato, T. Shirakawa, and S. Yunoki, *Phys. Rev. B* **91**, 125122 (2015).
- ³⁶ T. Sato, T. Shirakawa, and S. Yunoki, *arXiv:1603.01800* (2016).
- ³⁷ A. J. Kim, H. O. Jeschke, P. Werner, and R. Valentí, *Phys. Rev. Lett.* **118**, 086401 (2017).
- ³⁸ J. Terzic, J. C. Wang, Feng Ye, W. H. Song, S. J. Yuan, S. Aswartham, L. E. DeLong, S. V. Streltsov, D. I. Khomskii, and G. Cao, *Phys. Rev. B* **91**, 235147 (2015).
- ³⁹ G. Cao, V. Durairaj, S. Chikara, S. Parkin, and P. Schlottmann, *Phys. Rev. B* **75**, 134402 (2007).
- ⁴⁰ X. Liu, Vamshi M. Katukuri, L. Hozoi, Wei-Guo Yin, M. P. M. Dean, M. H. Upton, Jungho Kim, D. Casa, A. Said, T. Gog, T. F. Qi, G. Cao, A. M. Tsvelik, Jeroen van den Brink, and J. P. Hill, *Phys. Rev. Lett.* **109**, 157401 (2012).
- ⁴¹ G. Cao, J.E. Crow, R.P. Guertin, P.F. Henning, C.C. Homes, M. Strongin, D.N. Basov, and E. Lochner, *Solid State Comm.* **113**, 657 (2000).
- ⁴² M. A. Laguna-Marco, D. Haskel, N. Souza-Neto, J. C. Lang, V. V. Krishnamurthy, S. Chikara, G. Cao, and M. van Veenendaal, *Phys. Rev. Lett.* **105**, 216407 (2010).
- ⁴³ N. A. Bogdanov, Vamshi M. Katukuri, Hermann Stoll, Jeroen van den Brink, and Liviu Hozoi, *Phys. Rev. B* **85**, 235147 (2012).
- ⁴⁴ T. N. Nguyen and H.-C. zur Loye, *J. of Solid State Chem.* **117**, 300 (1995).
- ⁴⁵ K. Xiong, W. Liu, S. J. Teat, L. An, H. Wang, T. J. Emge, and J. Li, *J. of Solid State Chem.* **230**, 143 (2015).
- ⁴⁶ Y. Wang, D. Walker, B.-H. Chen, and B. A. Scott, *J. of Alloys and Compounds* **285**, 98 (1999).
- ⁴⁷ A. Abragam and B. Bleaney, *Electron Paramagnetic resonance of Transition Ions*, 1970.
- ⁴⁸ S. R. White, *Phys. Rev. Lett.* **69**, 2863 (1992).
- ⁴⁹ S. R. White, *Phys. Rev. B* **48**, 10345 (1993).
- ⁵⁰ S. R. White, *Phys. Rev. B* **72**, 180403(R) (2005).
- ⁵¹ D. Jerome, T.M. Rice, and W. Kohn, *Phys. Rev.* **158**, 462 (1967); B.I. Halperin and T.M. Rice, *Rev. Mod. Phys.* **40**, 755 (1968); B.I. Halperin and T. M. Rice, *Solid State Physics* **21**, 115 (1968).
- ⁵² L. Du, X. Sheng, H. Weng, and X. Dai, *Europhys. Lett.* **101**, 27003 (2013).
- ⁵³ J. Kuneš, *Journal of Physics: Condensed Matter*, Volume **27**, Number 33 (2015).
- ⁵⁴ T. Kaneko and Y. Ohta, *Phys. Rev. B* **90**, 245144 (2014).
- ⁵⁵ G. Khaliullin, *Phys. Rev. Lett.* **111**, 197201 (2013).
- ⁵⁶ S. Bhowal, S. Baidya, I. Dasgupta, and T. S. Dasgupta, *Phys. Rev. B* **92**, 121113(R) (2015).